



Synergy of oxygen vacancies and thermoelectric effect enhances uranium (VI) photoreduction

Pan He, Ling Zhang^{*}, Linzhen Wu, Shunhong Xiao, Xin Ren, Rong He, Xiaoyong Yang, Ruixi Liu, Tao Duan^{*}

State Key Laboratory of Environment-friendly Energy Materials, National Co-innovation Center for Nuclear Waste Disposal and Environmental Safety, Southwest University of Science and Technology, Mianyang 621010, Sichuan, China

ARTICLE INFO

Keywords:

Oxygen vacancy
Thermoelectric effect
Multi-field combination
Seebeck effect
U(VI) photoreduction

ABSTRACT

The conversion of soluble U(VI) to relatively immobilized U(IV) by photocatalytic techniques is considered to be the most effective method to prevent uranium contamination. Herein, a novel photocatalyst ($\text{TiO}_{2-x}/1\text{T-MoS}_2$) that combines photochemistry and thermoelectric physics is reported. The photocatalyst can use oxygen vacancies to briefly capture surrounding photogenerated electrons to improve the photogenerated carrier separation rate. Additionally, a large thermoelectric potential difference can be generated through a temperature gradient in the liquid environment, thereby changing the high-energy electron population on the substrate, and achieving the efficient capture of U(VI) species in extreme environments. The experimental results show that the $\text{TiO}_{2-x}/1\text{T-MoS}_2$ photocatalyst can remove more than 98% of U(VI) within 60 min without adding any sacrificial agent, and maintain a good U(VI) removal ratio even in a strong acid/base environment. This work will provide a reference for designing heterogeneous catalysts with both high catalytic activity and practicality for U(VI) photoreduction.

1. Introduction

The depletion of fossil fuel resources has led to the rapid development of nuclear energy, but this development has come with a series of environmental problems [1–3]. Most prominently, uranium in radioactive nuclear wastewater needs to be effectively removed because of its chemical toxicity and radioactivity that can cause permanent damage to the human body [4–6]. Fortunately, there are differences in solubility between uranium oxidation states, and so highly soluble hexavalent uranium [U(VI)] can be converted into relatively immobile tetravalent uranium [U(IV)] via photocatalytic techniques, allowing safer disposal [7–9]. However, the distribution of surface charges on the photocatalyst has a great influence on the efficient capture of U(VI) species [10–13]. Most of the reported semiconductor photocatalysts have weak surface charges, which makes them insufficient for U(VI) species capture and difficult to adapt to extreme environments such as strong acids/bases, resulting in poor U(VI) removal performance [14–16]. Utilizing the temperature gradient generated by the photocatalyst system in the liquid phase environment, the Seebeck effect is induced to generate a potential difference to accelerate the migration and population of

high-energy photogenerated electrons to the substrate, which can achieve the efficient capture of U(VI) species in extreme environments [17, 18]. Nevertheless, studies on such photocatalysis combined with thermoelectric effect are extremely rare. Therefore, it is urgent to study and design a multi-field driven photocatalyst for the efficient reduction of U(VI).

In 2011, Chen et al. reported for the first time that black TiO_{2-x} prepared by hydrogenation showed a high degree of photocatalytic activity [19]. This discovery sparked extensive, worldwide research into black TiO_{2-x} nanomaterials. Subsequently, Ye et al. prepared a series of TiO_x nanomaterials with different color gradients using the Mg reduction method, which resulted in a gradual increase in light absorption [20]. The essence of these methods was to adjust the concentration of O vacancies to prepare black TiO_{2-x} nanomaterials with small band gaps. Moreover, as a typical anion defect, many studies have shown that O vacancy can induce defect energy levels in the band gap to enhance the visible light absorption range and electron capture ability of the catalyst, so as to promote the effective separation and migration of photogenerated carriers [21–23]. Although great progress has been made in the preparation of pure black TiO_{2-x} , its photocatalytic reduction

^{*} Corresponding authors.

E-mail addresses: zhangling860817@163.com (L. Zhang), duant@ustc.edu.cn (T. Duan).

<https://doi.org/10.1016/j.apcatb.2022.122087>

Received 4 August 2022; Received in revised form 7 October 2022; Accepted 18 October 2022

Available online 19 October 2022

0926-3373/© 2022 Elsevier B.V. All rights reserved.

performance is still inadequate for practical application due to the lack of sufficient active sites, low separation rate of photogenerated carriers and insufficient utilization of environmental energy.

1T-phase transition metal dichalcogenides (TMDC), as low-dimensional materials, have been widely used as co-catalysts for photocatalysis and thermoelectric catalysis because of their excellent thermoelectric properties, abundant surface active sites, and high carrier mobility [24–27]. Achour et al. demonstrated that when a thermoelectric material was used as the substrate of the catalyst, the Fermi level of the catalyst could be changed through the thermoelectric effect, resulting in a significant improvement in the catalytic activity of the catalyst, and this phenomenon was called the thermoelectric promotion of catalysis (TEPOC) [17,28]. Stanley S. Chou et al. first observed the effectiveness of 1T-MoS₂ as a photothermal agent [29]. Huang et al. fabricated flexible p-type thermoelectric films based on 1T-MoS₂ nanosheets with a power factor in excess of 70 $\mu\text{W m}^{-1} \text{K}^{-2}$ at room temperature [26]. Despite such work, related research on thermoelectric materials as the substrate and the integration of the basic processes of photochemistry and thermoelectric physics remains extremely rare.

The coupling of semiconductor photocatalysts and co-catalysts can not only provide more active catalytic sites for the adsorption of uranyl, but also accurately regulate the unidirectional transfer of photogenerated electrons, which is considered to be the most traditional and effective method to achieve efficient charge separation [30–32]. Therefore, for this work, 1T-MoS₂ possessing thermoelectric properties was used as a substrate, which was coupled with the semiconductor photocatalyst TiO₂ to form a Schottky heterojunction with an ohmic contact. The unique work function difference between the two enabled the built-in electric field formed at the interface to significantly enhance the separation rate of photogenerated carriers and catalytic activity of photocatalysts. In addition, TiO_{2-x}/1T-MoS₂ photocatalysts with O vacancies were successfully prepared by exfoliating the surface lattice oxygen in TiO₂. From quantitative simulations, it was found that the O vacancy could induce the defect energy level in the band gap and be used as a shallow trap to briefly capture the surrounding photogenerated electrons. Not only that, the reduction of the tunneling barrier at the interface of the superlattice structure produces a larger thermoelectric potential difference, which changes the high-energy electron population on the 1T-MoS₂ surface, enabling efficient capturing of U(VI) species in extreme environments. These results demonstrated that the TiO_{2-x}/1T-MoS₂ photocatalyst could be driven by both light and thermal energy to remove 98.2% of U(VI) in the liquid phase system within 60 min, and maintain a good U(VI) removal ratio even in a strong acid/base environment. Synergy of oxygen vacancies and thermoelectric effect is an in-depth thinking on the effective combination of multiple energy fields, which is expected to further improve the utilization of energy. This work will provide a reference for designing heterogeneous catalysts with both high catalytic activity and practicality for U(VI) photoreduction.

2. Experimental section

2.1. Synthesis of TiO_{2-x}/1T-MoS₂ heterojunction

In a typical synthesis procedure, 0.084 g of MoO₃, 0.098 g of thioacetamide and 0.84 g of urea were dissolved in 70 mL of deionized water. After 30 min of sonication, 0.056 g of TiO₂ powder was added to the above solution and stirring was continued for 10 min. Subsequently, it was placed in a Teflon-lined stainless steel autoclave and heated at 180 °C for 12 h. The TiO₂/1T-MoS₂ heterojunctions were obtained by centrifugation and low temperature drying. Subsequently, TiO_{2-x}/1T-MoS₂ heterojunction were prepared using a chemical reduction method. The above 0.86 g of TiO₂/1T-MoS₂ powder was mixed with 1.204 g of sodium borohydride and ground until no odor was released. The mixture was placed in a tube furnace containing high purity Ar atmosphere at 350 °C for 60 min. After the reaction, the TiO_{2-x}/1T-MoS₂

heterojunction was obtained after washing with deionized water, centrifugation, and drying.

2.2. U(VI) photoreduction experiments

Unless otherwise specified, the concentration of U(VI) used in the experiments was 8 ppm and the solid-liquid ratio was 0.5 g L⁻¹. All experiments were performed at room temperature (T = 298 K). In the kinetic experiments, the adsorption capacity of the photocatalyst was evaluated according to the removal ratio of U(VI) in a dark environment (no external energy field). An appropriate amount of UO₂(NO₃)₂·6H₂O and photocatalyst were dissolved in deionized water, and the suspension with a solid-liquid ratio of 0.5 g L⁻¹ was gently stirred at room temperature (298 K) for 80 min without adding any sacrificial agent. During the reaction, take out an appropriate amount of supernatant at intervals of 5 min. After centrifugation to separate the solid phase and the liquid phase, the supernatant was filtered with a 0.22 μm filter membrane. The concentration of U(VI) in the obtained filtrate was determined by inductively coupled plasma optical emission spectrometry (Thermo Fisher, ICP-OES, ICAP7200). For comparison, photoreduction experiments were performed in a quartz reactor using a 300 W Xe lamp equipped as the photothermal source. The removal ratio was calculated by the following Eq. (1):

$$\text{U(VI) removal ratio(\%)} = \frac{(C_0 - C)}{C_0} \times 100\% \quad (1)$$

where C_0 (ppm) is the initial U(VI) concentration and C (ppm) is the residual U(VI) concentration. The immobilization ratio of U(VI) was calculated by the following Eq. (2):

$$\text{U(VI) immobilization ratio} = \text{U(VI) removal ratio} \times \frac{S_{\text{U(IV)}}}{S_{\text{total}}} \times 100\% \quad (2)$$

Where $S_{\text{U(IV)}}$ is the integral area of U(IV) in the XPS spectrum, and S_{total} is the total integral area of U. For the sake of investigate the effect of different organics and metal cations on the photoreduction of U(VI). In the organic interference experiments, 2 ppm methylene orange (Mo), methylene blue (MB), tributyl phosphate (TBP), methanol (Me), tannic acid (TA) and oxalic acid (OA) were mixed into 8 ppm U(VI), respectively. In the interference experiments of different valence metal cations, 40 ppm NaNO₃, KNO₃, Ca(NO₃)₂, Mg(NO₃)₂, Pb(NO₃)₂, and Eu(NO₃)₃ were used as suppliers of metal cations and were mixed into 8 ppm U(VI), respectively. Additionally, in order to explore the acid-base stability and optimal removal concentration of photocatalyst, a series of photocatalytic experiments were carried out in U(VI) solutions with different pH values and initial concentrations (8 ppm, 20 ppm, 40 ppm, 60 ppm, 80 ppm and 100 ppm). Other more detailed experiments and DFT calculations can be found in the [Supporting Information](#).

3. Results and discussion

3.1. Synthesis and characterizations

The precursor TiO₂/1T-MoS₂ was synthesized by a two-step hydrothermal method. Then, in the presence of the reducing agent NaBH₄, the TiO_{2-x}/1T-MoS₂ photocatalyst was obtained by annealing at 350 °C in a high-purity argon atmosphere (Fig. 1a). High-resolution transmission electron microscopy (HRTEM) and atomic force microscope (AFM) revealed the catalyst was composed of TiO_{2-x} nanosheets with an edge length and width of $\sim 50 \text{ nm} \times 40 \text{ nm}$ and a thickness of $\sim 8 \text{ nm}$ stacked on top of each other with wrinkled 1T-MoS₂ nanosheets (Fig. 1b, S1–S3). The superlattice interface formed by close stacking at the interface between the two was able to effectively increase the anharmonic scattering between phonons, thereby reducing the thermal conductivity (Fig. S4) [33,34]. Further magnification of the specific region revealed very clear lattice fringes with a spacing of approximately

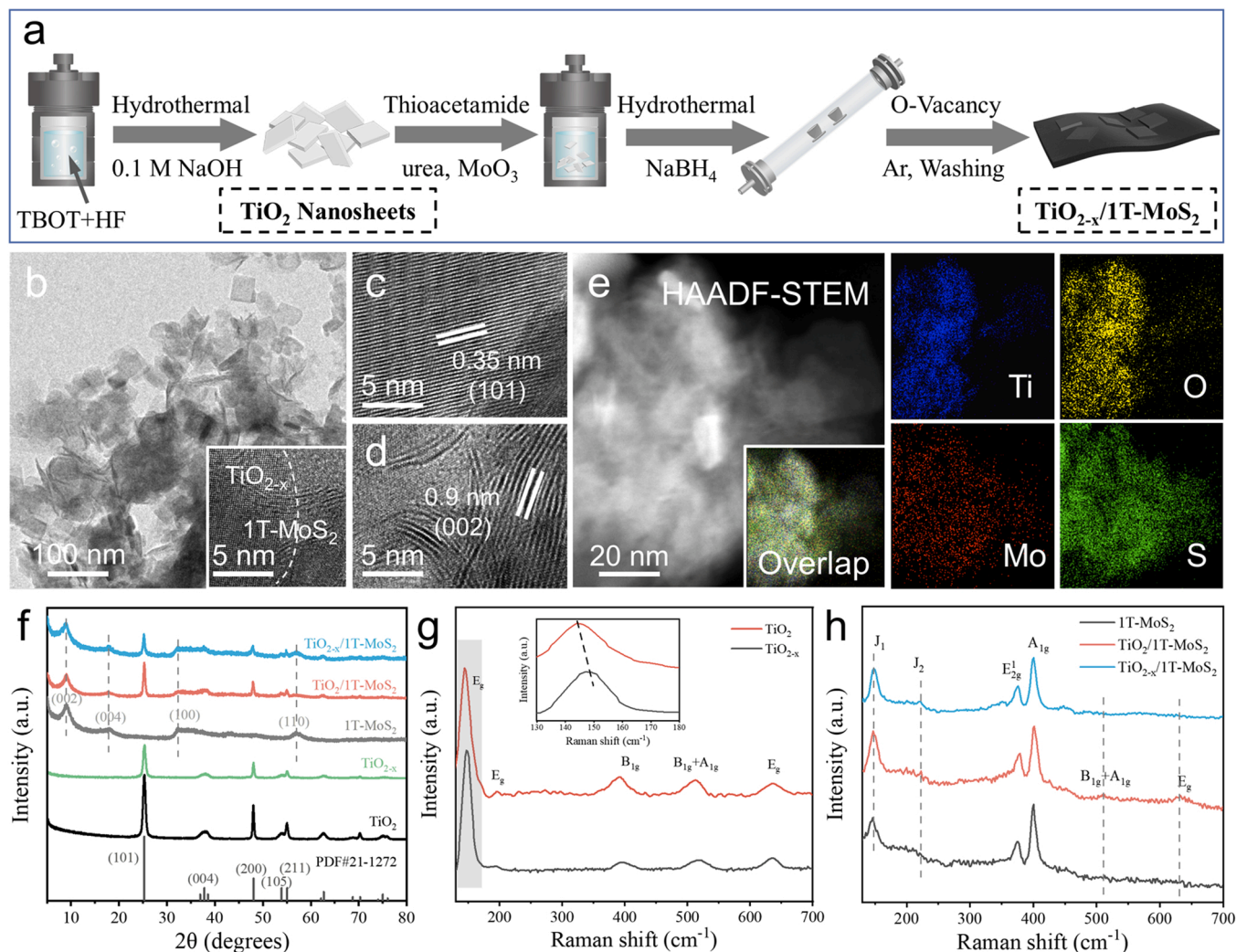


Fig. 1. (a) Schematic illustration of the synthesis process of the $\text{TiO}_{2-x}/1\text{T-MoS}_2$ heterojunction. TEM and HRTEM images of (b) $\text{TiO}_{2-x}/1\text{T-MoS}_2$, (c) TiO_{2-x} and (d) 1T-MoS_2 . (e) HAADF-STEM and corresponding EDS elemental mapping images of $\text{TiO}_{2-x}/1\text{T-MoS}_2$. (f) XRD patterns and (g-h) Raman spectra of the samples.

0.35 nm, which belonged to the (101) crystal plane of anatase TiO_2 (Fig. 1c) [35]. Additionally, the d-spacing of the (002) plane showed that the interlayer spacing of 1T-MoS_2 was about 0.9 nm (Fig. 1d) [36]. From the high-angle annular dark-field scanning transmission electron microscopy (HAADF-STEM) and the corresponding energy dispersive X-ray spectroscopy (EDS) (Fig. 1e), it can be seen that Ti and O elements were uniformly distributed across the 1T-MoS_2 substrate. These results showed that TiO_{2-x} was successfully loaded onto the 1T-MoS_2 substrate. The X-ray diffraction (XRD) patterns of the synthesized samples showed that the diffraction peak at 9.0° belongs to the typical (002) crystal plane of 1T-MoS_2 , which means the successful synthesis of 1T-MoS_2 (Fig. 1f) [37,38]. The presence of O vacancies caused lattice disorder in the TiO_2 crystal plane and led to a decrease in the overall crystallinity. In addition, the crystallinity and structure of the 1T-MoS_2 within the $\text{TiO}_{2-x}/1\text{T-MoS}_2$ photocatalyst were completely preserved after the annealing treatment at high temperature. In addition, the exfoliation of lattice oxygen in anatase TiO_2 shortened the adjacent Ti-O bond lengths around it, resulting in local structural disorder, as evidenced by the blue-shift of the E_g signal at low wavenumber positions (Fig. 1g) [39, 40]. More importantly, the MoS_2 of the 1T phase was metastable, so in the Raman spectrum shown in Fig. 1h, the J_1 and J_2 phonon modes belonging to the 1T phase and E_{2g}^1 and A_{1g} vibrational modes of the 2H phase appeared simultaneously [41]. Also, the strong Raman activity of the 2H phase made its vibrational modes very evident. With the

formation of the heterojunction, the $B_{1g} + A_{1g}$ and E_g vibrational signals belonging to anatase TiO_2 appeared in the Raman signal of $\text{TiO}_2/1\text{T-MoS}_2$, confirming the successful preparation of the heterojunction material. Meanwhile, the vibrational signal at this location in $\text{TiO}_{2-x}/1\text{T-MoS}_2$ was clearly weakened with the increase of O vacancies.

To further analyze the phase circumstance and chemical composition of $\text{TiO}_{2-x}/1\text{T-MoS}_2$, X-ray photoelectron spectroscopy (XPS) and electron paramagnetic resonance (EPR) were carried out on related samples. All elements could be found in the XPS overview spectra (Fig. 2a), which was consistent with the above analysis. More importantly, due to the spin-orbit splitting of the energy levels, two main peaks around 231.7 and 228.5 eV in the Mo 3d XPS spectra (Fig. 2b) were attributed to Mo 3d_{3/2} and Mo 3d_{5/2} of 1T-MoS_2 , respectively. Meanwhile, the two weak peaks around 232.8 eV and 229.4 eV were attributed to Mo 3d_{3/2} and Mo 3d_{5/2} of 2H- MoS_2 , respectively [42,43]. By calculating the ratio of the peak areas of the 1T and 2H phases, the content of the 1T phase was found to reach 71.3%, which means that the composition ratio of the 1T phase in the as-prepared 1T-MoS_2 nanosheets was high. After high temperature annealing, the content of 1T phase was still 65.2%, which could be well preserved. In addition, two small peaks appearing around 235.6 eV and 233.9 eV belonged to Mo^{6+} , which was caused by the oxidation of Mo edges [44]. Meanwhile, a single peak at 225.8 eV corresponded to the S^{2-} chemical state of MoS_2 [45]. Similarly, the characteristic peaks of 1T and 2H phase MoS_2 could also be deconvoluted in

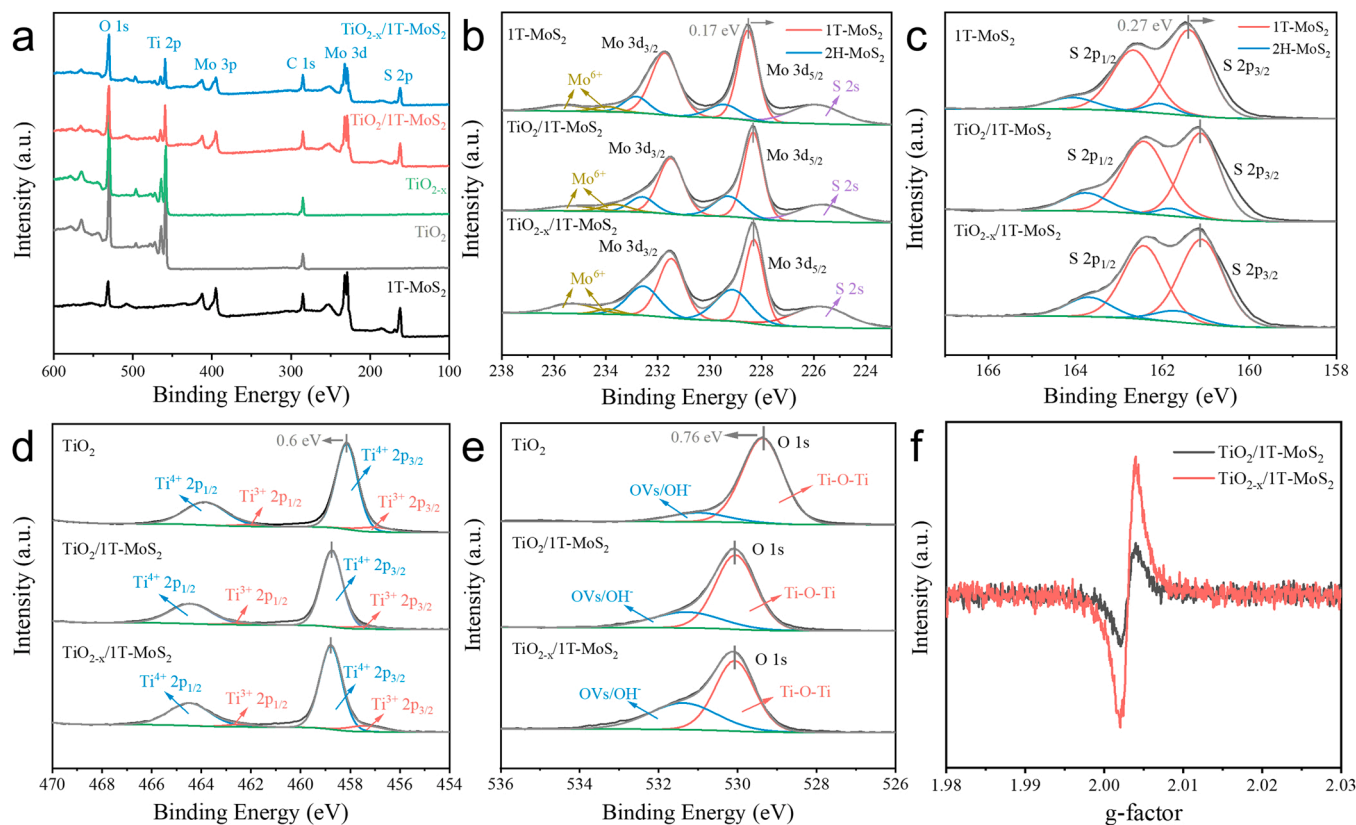


Fig. 2. (a) XPS overview spectra of the samples. High-resolution deconvolution XPS spectra of (b) Mo 3d, (c) S 2p, (d) Ti 2p and (e) O 1s (f) EPR spectra of $\text{TiO}_2/\text{1T-MoS}_2$ and $\text{TiO}_{2-x}/\text{1T-MoS}_2$.

the S 2p XPS spectra (Fig. 2c). Of particular interest were the shoulder peaks of Ti^{3+} and O vacancy, which were deconvoluted near 457.5 eV, 462.6 eV of the Ti 2p XPS spectra and 531.4 eV of the O 1s XPS spectra of the $\text{TiO}_{2-x}/\text{1T-MoS}_2$ (Fig. 2d and e), respectively. Due to the O vacancy may have induced the dissociation of H_2O and the chemisorption of OH^- in its vicinity, the binding energy of O in OH^- (531.4 eV) overlapped with the binding energy of the peak associated with the O vacancy [39]. Compared with other samples (Fig. S5b), $\text{TiO}_{2-x}/\text{1T-MoS}_2$ had the largest shoulder area, indicating more O vacancies existed on its surface. In contrast to pure 1T- MoS_2 , the binding energies of Mo 3d and S 2p orbitals of the composites both tended to shift towards lower binding energies. This means that after the heterojunction was formed, the electrons in the excited state were easily transferred from the TiO_{2-x} side over to 1T- MoS_2 , increasing the density of the surrounding electron cloud. On the contrary, the binding energies of the Ti 2p and O 1s orbitals of the composites both tended to shift towards high binding energies, indicating that the TiO_{2-x} side was prone to losing electrons. In the EPR spectrum (Fig. 2f), the O^- EPR signal around the g-factor of 2.003 was very obvious, which indicated that in the presence of the reducing agent NaBH_4 , annealing at high temperature could significantly increase the concentration of O vacancies. The difference was that no obvious Ti^{3+} EPR signal was found near the g-factor of 1.93 (Fig. S6), meaning it is possible that the excess surface charge associated with the bulk Ti^{3+} species diffused to the surface and generated O^- species after contact with O_2 in air, and thus only the O^- EPR signal appeared, but not that of Ti^{3+} EPR [46].

3.2. Energy band structure and charge-transfer properties

To gain a deeper understanding of the mechanism of the O vacancy-induced energy filtering effect, the energy band structures of the relevant samples were studied in detail. From the Tauc plot and UV-vis

diffuse reflectance spectra (UV-vis DRS) (Fig. 3a and Fig. S7), it could be seen that 1T- MoS_2 does not have a fixed absorption edge and can absorb visible light in a wide wavelength. Increasing the concentration of O vacancies can adjust the band gap value of TiO_2 to about 2.54 eV, and shift its absorption edge from 395 nm to 466 nm, thereby increasing its potential utilization of visible light. Further, ultraviolet photoelectron spectroscopy (UPS) was used to probe the work function and valence band position near the sample surface. From the results presented in Fig. 3b, it can be observed that the secondary electron cutoff (E_{cutoff}) energies of 1T- MoS_2 , TiO_2 , and TiO_{2-x} were 21.14, 16.14, and 16.82 eV, while the Fermi edge (E_F) values were 3.49, 2.08, and 1.96 eV, respectively. For metals, E_F coincides with the position of the top of the valence band, so the work function (ϕ_m) is calculated as $\phi_m = h\nu - E_{\text{cutoff}} + E_F$ [47]. For semiconductors, there is an energy difference between E_F and the top of the valence band, so in reality, the above formula calculates the position of the top of the valence band (E_v) of the semiconductor. Thus, the work function (ϕ_s) of the semiconductor is instead $\phi_s = h\nu - E_{\text{cutoff}}$ [13,48]. Based on the aforementioned, the schematic diagrams of the band structures of 1T- MoS_2 , TiO_2 , and TiO_{2-x} are provided in Fig. 3c. The metal phase 1T- MoS_2 had a lower work function (3.57 eV), and when it was in close contact with TiO_2 with a higher work function (5.08 eV), the electrons transferred from 1T- MoS_2 to the TiO_2 side to form a built-in electric field. Specifically, the accumulation of electrons on the side of TiO_2 bent the energy band near its contact surface downward and formed a typical ohmic contact with the metallic phase 1T- MoS_2 . The formation of this built-in electric field and ohmic contact could effectively promote the migration of photogenerated electrons to the 1T- MoS_2 side, thereby significantly increasing the separation rate of photogenerated carriers. However, the large bandgap value of 3.13 eV of pure TiO_2 could not effectively promote more electronic transitions. More importantly, its high electron affinity ($\chi = 4.03$ eV) enabled the heterojunction interface to occur with a large

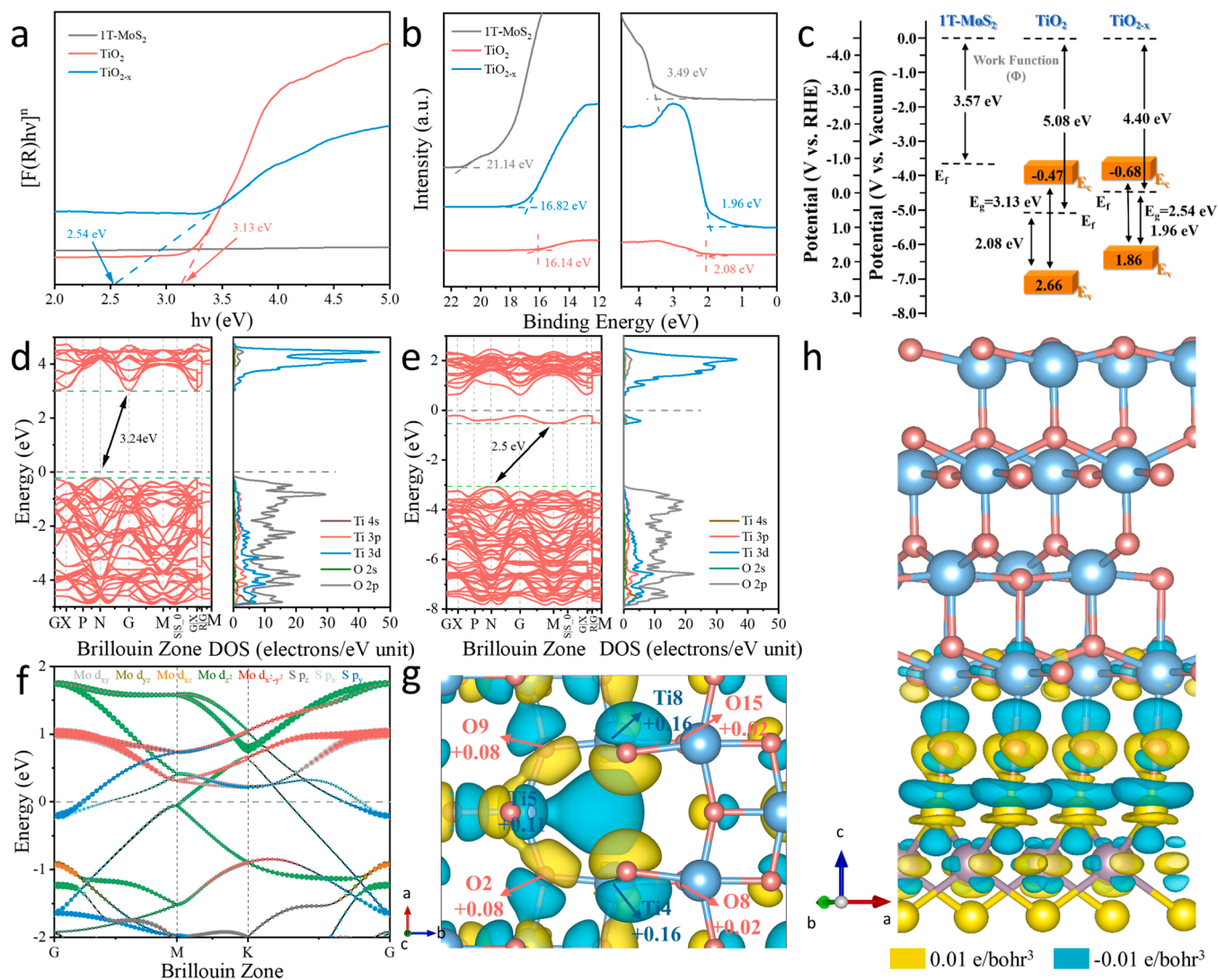


Fig. 3. (a) Tauc plots and (b) UPS spectra of 1T-MoS₂, TiO₂ and TiO_{2-x}. (c) Schematic energy band diagrams of 1T-MoS₂, TiO₂ and TiO_{2-x} before contact. E_F , Fermi level; E_c , conduction band position; E_v , valence band position; E_g , bandgap value. The calculated band structures and density of states of (d) TiO₂ and (e) TiO_{2-x}. (f) Orbital projection of the band structure of 1T-MoS₂. (g) Charge distribution in TiO_{2-x}. The yellow and cyan regions represent charge accumulation and depletion, respectively. (h) Charge density difference plot at the TiO_{2-x}/1T-MoS₂ interface. Blue atoms represent Ti atoms, red atoms represent O atoms, purple atoms represent Mo atoms and yellow atoms represent S atoms.

barrier height ($V_B = 0.46$ eV) (Fig. S8). An excessively high tunnel barrier may prevent the propagation of some high-energy electrons, leading to a decrease in the average electron kinetic energy, which would undoubtedly reduce the Seebeck coefficient of the system material [34,49,50]. Fortunately, we found through experiments that O vacancies could not only lower the value of the band gap, but also significantly reduce the barrier height of the interface by reducing the electron affinity ($V_B = 0.25$ eV). This could significantly improve the Seebeck coefficient of the photocatalyst, thereby enabling more efficient multi-field-driven photoreduction.

In order to further clarify the effect of O vacancies on the photocatalyst and the source of the conductive properties of 1T-MoS₂, we calculated the band structures of TiO₂ and TiO_{2-x} and the atomic orbital projections of 1T-MoS₂ using HSE hybrid functional. The distribution and transfer of electrons in TiO_{2-x}/1T-MoS₂ were simulated by single-point calculation. As shown in Fig. 3d and e, the band gap values (E_g) of TiO₂ and TiO_{2-x} were 3.24 and 2.50 eV, respectively. Notably, the valence band maximum and conduction band minimum of the two were not at the same position in k-space, which means that the photo-generated electrons would be scattered by the lattice during the de-

excitation process and emit phonons. This allowed part of the light energy to be released to the surroundings as heat. The difference was that the number of energy bands on TiO_{2-x} was denser than that of TiO₂, which indicates that there were more atomic orbitals involved in hybridization in TiO_{2-x} and the localization of electrons was more evident [51]. Furthermore, O vacancies made TiO_{2-x} excite defect levels near the Fermi level. As a ladder for electronic transitions, this defect level enabled electrons to undergo two transitions, further reducing the total energy of photoexcited carrier transitions. This phenomenon was consistent with the results for the two absorption bands observed in Fig. S7 (near-UV absorption region at 250–466 nm and a tail-like absorption band at 466–700 nm) [22,23]. It is not difficult to find from the density of state (DOS) diagram that the defect energy level was mainly contributed by the electrons on the Ti 3d orbital. Combined with Fig. 3g, it could be seen that the absence of lattice oxygen caused a redistribution of charge around the surrounding Ti and O atoms, and the Ti atom regained the most electrons. More importantly, the redistribution of charges caused the 3d orbitals of the 3 Ti atoms closest to the O vacancy contained unpaired electrons to form unsaturated covalent bonds and existed in the form of electron gas (Fig. S9), these bonds tended to accept

electrons so that the O vacancy acted as an acceptor and attracted surrounding electrons. The implication of this was that O vacancies can be used as a shallow defect to temporarily capture photogenerated electrons to prolong the lifetime of photogenerated electrons, and increase the separation rate of photogenerated carriers. The relative effective masses of electrons and holes in TiO_2 and TiO_{2-x} were further calculated using Eq. (3) as below:

$$\frac{1}{m^*} = \frac{1}{\hbar^2} \frac{\partial^2 E(k)}{\partial k^2} \quad (3)$$

where m^* is the relative effective mass, \hbar is the reduced Planck constant, and $E(k)$ is the energy of an electron at wavevector k in that band [52]. Compared to TiO_2 , the lower relative effective mass of electrons in TiO_{2-x} corresponds to higher electron mobility (Table S1), and the large difference between the relative effective masses of electrons and holes corresponds to a low recombination rate between electron and hole pairs [23]. In a noteworthy result, as seen from the molecular orbital projection of 1T-MoS₂ (Fig. 3f), the O_h-MoS₆ complex in the 1T-MoS₂ primary cell divided the Mo 4d orbitals into three groups: an occupied doubly degenerate E_g set (4d_{xz} and 4d_{yz}), an unoccupied doubly degenerate E_g set (4d_{xy} and 4d_{x²-y²}), and a partially occupied non-degenerate A_{1g} set (4d_{z²}). Among them, the partially occupied split Mo 4d_{z²} orbital crossed the fermi level resulting in metallic conductivity in 1T-MoS₂. In addition to this, the fermi level passed through the double degenerate set S 3p_x and 3p_y at the G point with an integral area of approximately 0.055 (grey area), which represented the electron concentration (Fig. S10). Conversely, crossing the split Mo 4d_{z²} orbital at the K point resulting in an integral area of about 0.09 (orange area), denoting the hole concentration. According to the free electron model, the density of free holes was greater than that of free electrons, so 1T-MoS₂ exhibited p-type conductivity [26]. We determined the optimal contact mode of $\text{TiO}_{2-x}/\text{1T-MoS}_2$ by comparing the adsorption energies. As shown in Fig. S11 and Table S2, The adsorption energy at O-S side contact of -10.44 eV was significantly smaller than -7.19 eV for Ti-S

side contact, which indicates that O-S side contact occurred more easily. Based on this, the charge distribution at the contact interface of the heterojunction was investigated using charge density difference and bader topological calculation. A clear charge redistribution phenomenon was observed from Fig. 3h, the electrons accumulated on the TiO_{2-x} side. It was found by bader topological calculation (Table S3) that each 1T-MoS₂ unit cell transferred 3.2 e⁻ to a corresponding TiO_{2-x} unit cell. The accumulation of electrons on the TiO_{2-x} side made the 1T-MoS₂ side positively charged and formed a built-in electric field near the contact interface, which could promote the separation of photogenerated carriers.

The interband transitions and migration directions of photogenerated electrons directly affect the photocatalytic performance, so the dynamic characteristics of the photogenerated electrons were further analyzed by electrochemical and photophysical characterization. Fig. 4a shows the Nyquist plots of some samples, combined with the energy band analysis, it can be seen that O vacancies indirectly increase the metallicity of the photocatalyst by reducing the distance between the fermi energy level and the conduction band. The introduction of O vacancies and metallic phase 1T-MoS₂ enabled $\text{TiO}_{2-x}/\text{1T-MoS}_2$ to have the smallest resistance semicircle, which guaranteed the rapid transfer of electrons at its interface [53]. Similarly, in the transient photocurrent responses test (Fig. 4b), the $\text{TiO}_{2-x}/\text{1T-MoS}_2$ exhibited the highest photocurrent density, which implies more efficient carrier transfer and separation. To provide tangible proof of the transfer of photogenerated electrons from TiO_{2-x} to 1T-MoS₂, the spatial distribution of charges at the interface was analyzed using Kelvin probe force microscopy (KPFM) (Fig. 4c-e). In the atomic force microscope image (AFM), the position of the red dashed box was marked as 1T-MoS₂ (marked as A), and the position of the blue dashed box was marked as TiO_{2-x} (marked as B). By comparing the surface photovoltage spectra (SPV) in the dark and photothermal conditions, the potential at the A site decreased by ~7 mV, while the potential at the B site increased by ~4 mV in the photothermal conditions, indicating a spatial migration process of photogenerated electrons from the B site to the A site [54–56]. This

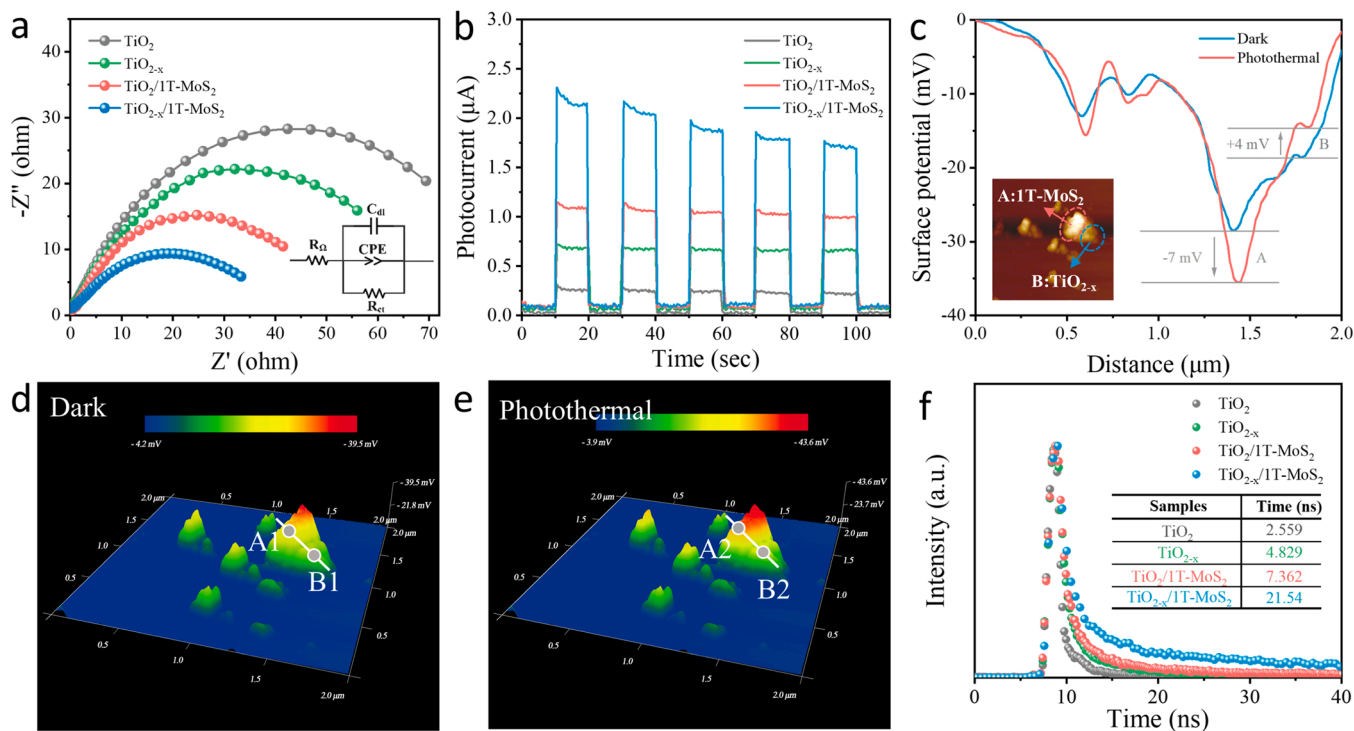


Fig. 4. (a) Electrochemical impedance spectroscopy and (b) Transient photocurrent responses of the samples. (c) Surface photovoltage in the dark and photothermal conditions and AFM topography of $\text{TiO}_{2-x}/\text{1T-MoS}_2$. (d) Surface photovoltage distribution of $\text{TiO}_{2-x}/\text{1T-MoS}_2$ in the dark and (e) photothermal conditions. (f) Time-resolved PL spectra of the samples.

directional electron migration process increased the separation rate of photogenerated carriers. The process can be seen more intuitively through the surface photovoltage distribution diagram. More importantly, in the time-resolved photoluminescence spectra (TRPL) (Fig. 4f), the dynamics of these samples accorded with a second-order exponential decay behavior. Due to the presence of O vacancies, the lifetime of photogenerated electrons generated by TiO_{2-x} was 1.9 times longer than that of TiO_2 . Furthermore, the introduction of O vacancies and the metallic phase 1T-MoS₂ increased the photogenerated electron lifetime of the $\text{TiO}_{2-x}/1\text{T-MoS}_2$ heterojunction to an astonishing 21.54 ns. The phenomenon can be attributed to the temporary trapping of photogenerated electrons by O vacancies and the efficient transfer of photogenerated electrons by the metallic phase 1T-MoS₂. The significant increase in the lifetime of the photogenerated electrons implies an increase in the separation rate of photogenerated carriers, which helps to improve the catalytic activity of the photocatalyst for more efficient U (VI) photoreduction.

3.3. Thermoelectric properties

The Seebeck effect induced by temperature gradient was used to separate photogenerated carriers and achieve multiple efficient utilization of energy in liquid environment, which puts forward certain requirements for the thermoelectric performance of photocatalysts. Therefore, we investigated the mechanism of the Seebeck effect by using phonon spectrum, thermal conductivity, Seebeck coefficient and time-temperature dependence curve. The phonon dispersions between the high frequency optical model and the low frequency acoustic mode of 1T-MoS₂ showed distinct imaginary modes near the M and K points (Fig. 5a). The indelible imaginary modes indicated the thermodynamic instability of 1T-MoS₂ (Fig. S12), which may be caused by the deviation of the equilibrium position of the Mo atom from the energy minimum after violent vibration. In addition, the three lowest phonon branches could be branched at the Γ point: the out-of-plane acoustic mode (ZA), the in-plane transverse acoustic mode (TA), and the in-plane

longitudinal acoustic mode (LA) [57]. The existence of the forbidden band between the high-frequency optical branch and the low-frequency acoustic branch means that the material has a high lattice thermal conductivity, which is unfavorable for the improvement of the Seebeck effect [58,59]. Fortunately, in the phonon dispersions of $\text{TiO}_2/1\text{T-MoS}_2$ (Fig. 5b), the existence of the superlattice interface enabled a strong interaction between the low-frequency segment of the optical branch and the high-frequency segment of the acoustic branch, which could greatly reduce the group velocity of high-frequency acoustic phonons and the thermal conductivity of the material lattice. The local lattice distortion caused by the introduction of O vacancies slightly weakens this strong interaction (Fig. 5c). The thermoelectric properties of some samples were measured in the temperature range of 300–500 K. As shown in Fig. 5d, the thermal conductivity of the composite photocatalyst was significantly lower than that of the metallic phase 1T-MoS₂, which represents a larger thermal resistance inside the system. Compared with $\text{TiO}_2/1\text{T-MoS}_2$, the thermal conductivity of $\text{TiO}_{2-x}/1\text{T-MoS}_2$ increased slightly, but after the temperature reached 400 K, the difference gradually decreased. The thermal conductivity measurements were in good agreement with the previously simulated phonon dispersion results. It was worth noting that the thermal conductivities of all samples showed a clear increasing trend after the temperature exceeded 400 K, which could be attributed to a decrease in the content of 1T phase MoS₂ caused by the transition of metastable 1T-MoS₂ to stable 2H-MoS₂ [26,60]. By analyzing the temperature-dependent Seebeck coefficient (Fig. 5e) and local density of state (LDOS) (Fig. S13), the mechanism of the enhancement of the Seebeck effect was clarified. The introduction of n-type TiO_2 provides additional electrons for the system materials to increase the density of states per unit space electrons, which increases the Seebeck coefficient from 35.4 $\mu\text{V K}^{-1}$ to 75.2 $\mu\text{V K}^{-1}$ at room temperature. More importantly, the presence of O vacancies further increases the Seebeck coefficient of the $\text{TiO}_{2-x}/1\text{T-MoS}_2$ heterojunction to 82.3 $\mu\text{V K}^{-1}$. This is because the O vacancy reduced the electron affinity by shifting the fermi energy level up, thereby further reducing the height of the tunnel barrier at the

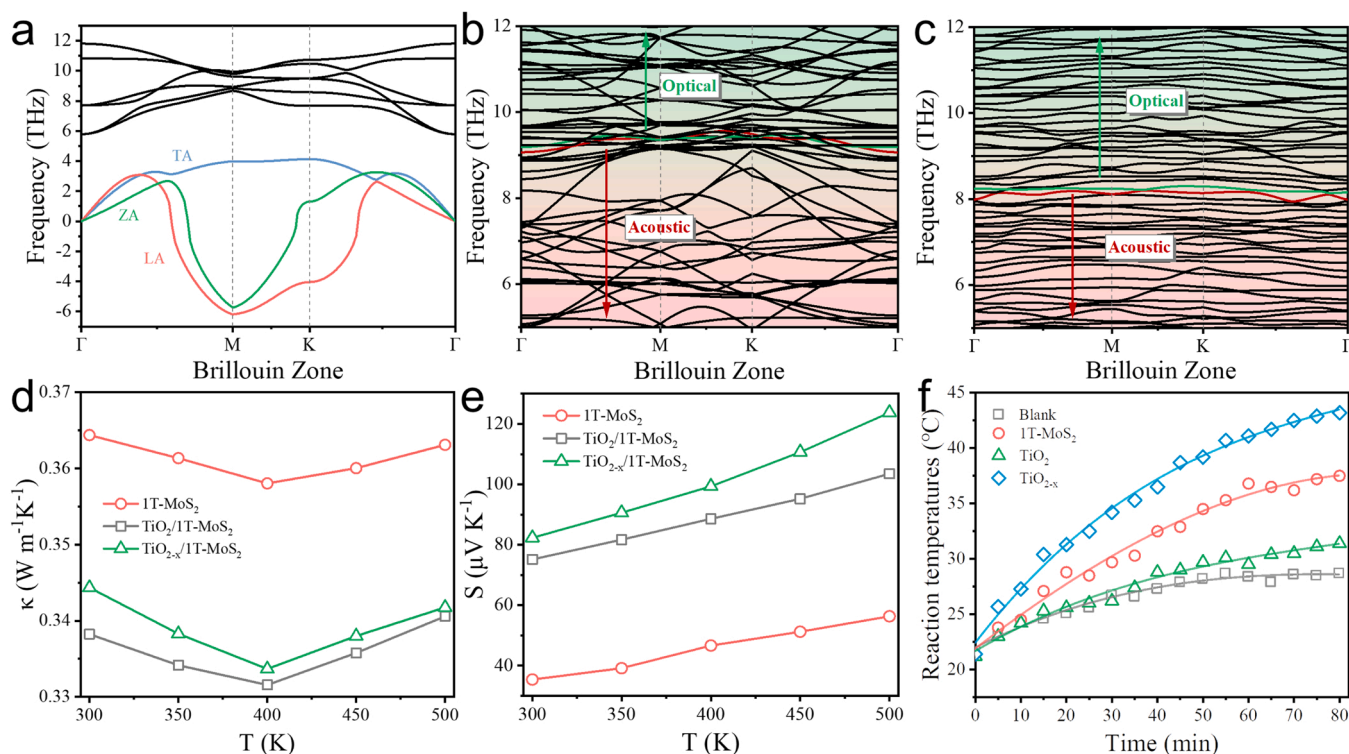


Fig. 5. Phonon dispersions for (a) 1T-MoS₂, (b) TiO₂/1T-MoS₂ and (c) TiO_{2-x}/1T-MoS₂. The temperature-dependent (d) thermal conductivity and (e) Seebeck coefficient. (f) Time-temperature dependence curves of different photocatalysts.

heterojunction interface and realizing more effective low-energy electron filtering. Suppressing the electron population of low-energy electrons would increase the average electron kinetic energy of high-energy electrons, leading to an increase in the Seebeck coefficient. This process can generate a larger potential difference to promote the migration of high-energy photogenerated electrons to the metallic phase 1T-MoS₂. In order to verify the temperature difference between the two sides of the heterojunction, we used an infrared thermometer to measure the time-temperature dependence curves of select samples during the reaction. As shown in Fig. 5f, there was a clear liquidus temperature difference between 1T-MoS₂ and TiO_{2-x} as the reaction time increased. This means that in the TiO_{2-x}/1T-MoS₂ heterojunction, TiO_{2-x} would act as the hot end and 1T-MoS₂ as the cold end. Under this temperature gradient, the electrons generated by thermal excitation moved from the hot end to the cold end, and a potential differential was formed inside the material, which in turn promoted the migration of electrons generated by photoexcitation to the 1 T-MoS₂ side. It was worth noting that the temperature difference between TiO₂/1T-MoS₂ and TiO_{2-x}/1T-MoS₂ within 80 min wasn't too great (less than 2.5 K) (Fig. S14), but TiO_{2-x}/1T-MoS₂ was slightly higher than TiO₂/1T-MoS₂. This result was consistent with the measurement of TiO_{2-x}/1T-MoS₂ having higher total

thermal conductivity than TiO₂/1T-MoS₂ in Fig. 5d.

3.4. Uranium photoreduction experiments

To verify the outstanding contribution of the synergy of oxygen vacancies and thermoelectric effect to the multi-field-driven U(VI) photoreduction, the kinetics of U(VI) removal for the as-prepared samples driven by different energy fields were investigated. Under dark conditions (no external energy field) (Fig. 6a), 1T-MoS₂ achieved 25.6% physical adsorption of U(VI) in a liquid phase environment due to its large specific surface area. Compared with TiO₂ and TiO₂/1T-MoS₂, the removal ratios of U(VI) by TiO_{2-x} and TiO_{2-x}/1T-MoS₂ both increased, reaching 23.4% and 35.6%, respectively. In the longitudinal comparison of the light field-driven experiment (Fig. S15a), the presence of O vacancies in the TiO_{2-x}/1T-MoS₂ composite improved the performance of the photocatalyst to 82.4% compared with that of TiO₂/1T-MoS₂. This was undoubtedly caused by the temporary capture of photogenerated electrons by unsaturated covalent bonds near O vacancies, which increased the lifetime of photogenerated electrons. Additionally, in the thermal field-driven experiment (Fig. S15b), the removal ratio of U(VI) by TiO_{2-x}/1T-MoS₂ composite could reach 73.0% thanks to the larger

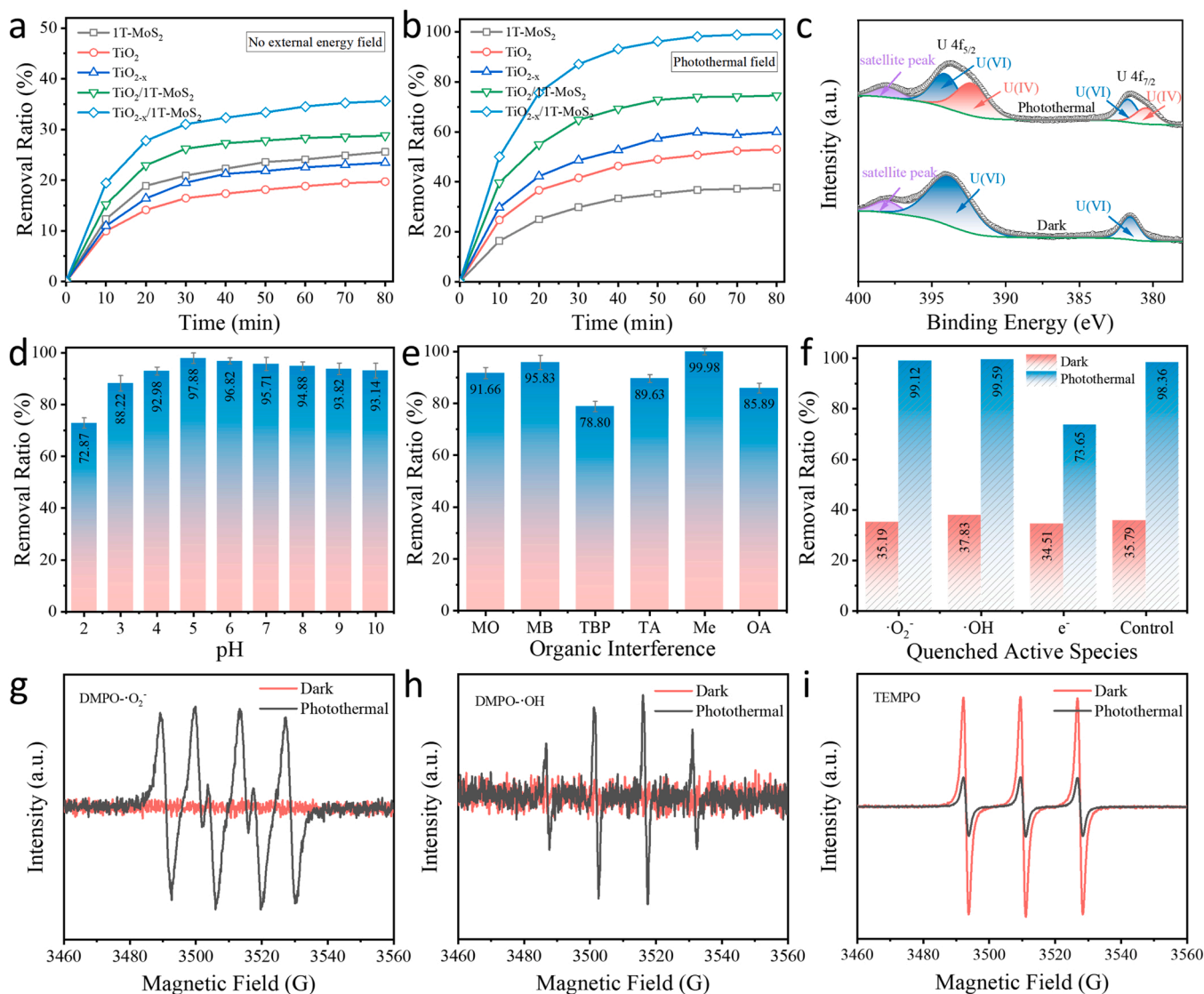


Fig. 6. Reaction kinetics of the samples in the (a) dark (no external energy field) and (b) photothermal field. (c) U 4f spectra of TiO_{2-x}/1T-MoS₂ in the dark and photothermal conditions. (d) Effect of pH on the TiO_{2-x}/1T-MoS₂. (e) Removal ratios of U(VI) by TiO_{2-x}/1T-MoS₂ under the condition that different organics coexist with U(VI). (f) The active species (·O₂⁻, ·OH and e⁻) capture experiments. ESR signals of (g) DMPO-·O₂⁻, (h) DMPO-·OH and (i) TEMPO adducts over TiO_{2-x}/1T-MoS₂.

thermoelectric potential difference caused by the reduction of tunneling barrier. The difference was that the synergy of oxygen vacancies and thermoelectric effect was induced in the photothermal field to further enhance the U(VI) removal ratio to nearly 98.2% in the liquid phase system within 60 min (Fig. 6b). The U(VI) removal performance of different reported photocatalysts were compared in Table S4. This excellent removal performance is attributed to the synergy of oxygen vacancy and thermoelectric effect. As shown in Fig. 6c, we investigated the U(VI) immobilization process of $\text{TiO}_{2-x}/1\text{T-MoS}_2$ by deconvoluting XPS spectra of U4f in the dark and photothermal conditions. Unexpectedly, a satellite peak due to energy loss appeared at 398.1 eV. In dark conditions, almost all of the uranium species deposited on the surface of the $\text{TiO}_{2-x}/1\text{T-MoS}_2$ photocatalyst were U(VI). In contrast, both U(VI) and U(IV) species appeared on the surface of the $\text{TiO}_{2-x}/1\text{T-MoS}_2$ photocatalyst after being driven by photothermal. By calculating the integral area of U(VI) and U(IV) species (Fig. 6c and S16), 49.0% of U(IV) was immobilized on the surface of $\text{TiO}_{2-x}/1\text{T-MoS}_2$ (22.5% on the surface of $\text{TiO}_2/1\text{T-MoS}_2$). From the EDS elemental mapping images of $\text{TiO}_{2-x}/1\text{T-MoS}_2$ (Fig. S17), it can be clearly seen that the U element was evenly distributed on the surface of $\text{TiO}_{2-x}/1\text{T-MoS}_2$. Compared with $\text{TiO}_2/1\text{T-MoS}_2$, the O vacancy reduced the electron affinity and made $\text{TiO}_{2-x}/1\text{T-MoS}_2$ have a higher thermoelectric potential difference, which directly led to higher U(VI) removal ratio of $\text{TiO}_{2-x}/1\text{T-MoS}_2$. The pH in the liquid environment affects the photoreduction process by affecting the form of U(VI) ions present. As shown in Fig. 6d, the photocatalyst exhibited over 90% U(VI) removal at pH ranging from 4 to 10. The difference was that when the liquid environment was too acidic, the phenomenon that H^+ and H_3O^+ competed with U(VI) for surface active sites becomes apparent, resulting in a sharp decline in the performance of the $\text{TiO}_{2-x}/1\text{T-MoS}_2$ photocatalyst [31]. To further simulate real nuclear wastewater, in this work, the effects of multiple different organics and variable valence cations on the removal efficiency of photocatalysts were investigated. As shown in Fig. 6e, the removal of U(VI) was 91.7% due to the electrostatic repulsion between UO_2^{2+} and positively charged methylene orange (Mo) molecules [61]. It is worth noting that the presence of tributyl phosphate (TBP) had an obvious effect on U(VI) removal, which may be because TBP affected the binding of electrons and U(VI). Not only that, Tannic acid (TA) and oxalic acid (OA), as macromolecular organics, might compete with U(VI) for surface adsorption/photoreduction sites, thus slightly affecting the efficiency of U(VI) removal. The difference was that methanol (Me), as a typical hole sacrificial agent, could suppress the recombination of photogenerated carriers by consuming holes to improve the removal ratio of U(VI) [62]. In addition, the $\text{TiO}_{2-x}/1\text{T-MoS}_2$ photocatalyst could still maintain a high U(VI) removal ratio when 5 times the variable valence metal cations coexist with U(VI) (such as Na^+ , K^+ , Ca^{2+} , Mg^{2+} , Pb^{2+} and Eu^{3+}) (Fig. S18), respectively. The samples also attained satisfactory results at different solid-liquid rate (Fig. S19), and when the solid-liquid ratio was greater than 1:4, a removal ratio of more than 92.4% could be reached. Surprisingly, in different initial concentration experiments of U(VI) (Fig. S20), the $\text{TiO}_{2-x}/1\text{T-MoS}_2$ photocatalyst exhibited higher U(VI) removal ratio in a wide concentration range. Based on the above results, we utilized ESR spectra to verify the existence of $\cdot\text{O}_2^-$, $\cdot\text{OH}$ and photogenerated electrons reactive radical species. The ESR signals of $\text{DMPO}\cdot\text{O}_2^-$ and $\text{DMPO}\cdot\text{OH}$ formed distinct characteristic peaks under the photothermal condition (Fig. 6g and h), which means that the $\text{TiO}_{2-x}/1\text{T-MoS}_2$ photocatalyst produced $\cdot\text{O}_2^-$ and $\cdot\text{OH}$ radicals during the reaction. Nevertheless, the ESR signal of TEMPO was significantly weakened after being driven by photothermal (Fig. 6i), which proved the generation of photogenerated electrons (TEMPO was directly reduced to TEMPOH by the photogenerated electrons) [42,63]. Furthermore, we used p-benzoquinone (P-BQ) as radical scavengers of $\cdot\text{O}_2^-$, isopropyl alcohol (IPA) as radical scavengers of $\cdot\text{OH}$ and sodium persulfate ($\text{Na}_2\text{S}_2\text{O}_8$) as radical scavengers of e^- to study the main reactive radical species during the photoreduction of U(VI). As shown in Fig. 6f, the addition of $\cdot\text{O}_2^-$ and $\cdot\text{OH}$ radical scavengers did not

significantly affect the removal of U(VI). The difference was that the removal ratio of U(VI) by $\text{TiO}_{2-x}/1\text{T-MoS}_2$ showed a downward trend under the photothermal condition. From the ESR spectra and active species capture experiments, it can be seen that photogenerated electrons participated in the photoreduction of U(VI) as the main active species in the reaction process.

In order to more intuitively understand the transfer mechanism of photogenerated electrons in the photocatalytic process, a detailed schematic diagram of the process is shown in Fig. 7. Firstly, after the electrons with sufficient energy are transitioned to the conduction band to become photogenerated electrons, there is a certain probability that they will be captured by the unsaturated covalent bonds near the oxygen vacancy. But the defect level induced by oxygen vacancies is shallow energy level, so this capturing is short-lived. Secondly, since a significant temperature gradient is formed near the heterojunction interface in the liquid-phase environment, a thermoelectric potential difference is generated through the Seebeck effect. This allows more escaped photogenerated electrons and other photogenerated electrons to be transferred to the substrate surface. Finally, the photogenerated electrons that escaped to the substrate surface achieved thorough spatial separation, and then participated in the capture and photoreduction of uranyl ions. In conclusion, this thermoelectric effect assisted the photocatalytic process provides potential possibilities for the efficient photoreduction of U(VI) and its application in extreme environments.

4. Conclusion

In summary, in terms of photochemistry, O vacancies not only reduced the band gap value of the photocatalyst and improved the utilization of visible light, but also acted as a shallow trap to improve the separation rate of photogenerated carriers by briefly capturing surrounding photogenerated electrons. In terms of thermoelectric physics, the contact interface of the $\text{TiO}_{2-x}/1\text{T-MoS}_2$ photocatalyst produced a temperature gradient in the liquid phase environment, and the potential difference was generated by the Seebeck effect to change the population of high-energy photogenerated electrons on the substrate to achieve efficient capture of U(VI) species in extreme environments. The experimental results demonstrated that the $\text{TiO}_{2-x}/1\text{T-MoS}_2$ photocatalyst could be driven by both light and thermal energy. The $\text{TiO}_{2-x}/1\text{T-MoS}_2$ photocatalyst achieved over 98% removal of U(VI) within 60 min without adding any sacrificial agent, and maintain a good U(VI) removal ratio even in a strong acid/base environment. Not only that, the high removal ratio of U(VI) could still be maintained in the presence of various competitive cations and organic pollutants. Synergy of oxygen vacancies and thermoelectric effect is an in-depth thinking on the effective combination of various energy fields, which is expected to further improve the utilization of energy. It is considered that the results of this work will provide a reference for designing heterogeneous catalysts with both high catalytic activity and practicality for U(VI) photoreduction.

CRediT authorship contribution statement

Pan He: Conceptualization, Methodology, Theoretical calculations, Writing – original draft, Writing – review & editing. **Ling Zhang:** Supervision, Resources. **Linzheng Wu, Shunhong Xiao, Xin Ren, Ruixi Liu:** Methodology, Validation. **Rong He:** Writing – review & editing. **Xiaoyong Yang:** Theoretical calculations. **Tao Duan:** Project administration, Funding acquisition, Writing – review & editing.

Declaration of Competing Interest

The authors declare that they have no known competing financial interests or personal relationships that could have appeared to influence the work reported in this paper.

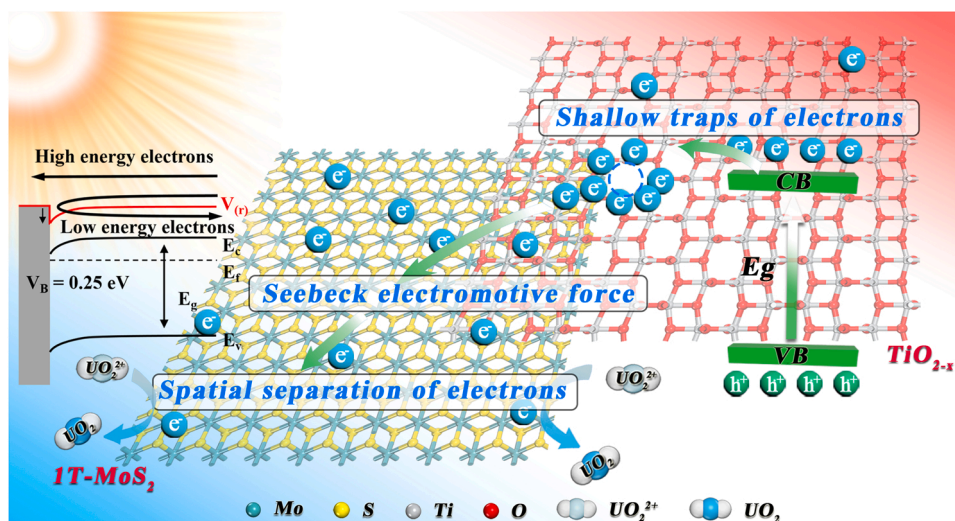


Fig. 7. Mechanism of photogenerated electron transfer during photocatalysis.

Data availability

Data will be made available on request.

Acknowledgments

This work was supported by the National Natural Science Foundation of China (No. 21976148, 21906133, 11905177, 21902129); the Basic Scientific Research Project of China (No. JCKY2018404C008); the National Key Research and Development Project of China (No. 2016YFC1402500); the Project of State Key Laboratory of Environment-friendly Energy Materials in SWUST (No. 18zxhk04). The authors would like to express their thanks to Suzhou Deyo Bot Advanced Materials Co., Ltd. (www.szdybc.com) for providing support on material characterization.

Appendix A. Supporting information

Supplementary data associated with this article can be found in the online version at doi:10.1016/j.apcatb.2022.122087.

References

- C. Wang, A.S. Helal, Z. Wang, J. Zhou, X. Yao, Z. Shi, Y. Ren, J. Lee, J.-K. Chang, B. Fugetsu, J. Li, Uranium in situ electrolytic deposition with a reusable functional graphene-foam electrode, *Adv. Mater.* 33 (2021) 2102633.
- T. Chen, B. Liu, M. Li, L. Zhou, D. Lin, X. Ding, J. Lian, J. Li, R. He, T. Duan, W. Zhu, Efficient uranium reduction of bacterial cellulose-MoS₂ heterojunction via the synergistically effect of Schottky junction and S-vacancies engineering, *Chem. Eng. J.* 406 (2021), 126791.
- Y. Zhang, M. Zhu, S. Zhang, Y. Cai, Z. Lv, M. Fang, X. Tan, X. Wang, Highly efficient removal of U(VI) by the photoreduction of SnO₂/CdCO₃/CdS nanocomposite under visible light irradiation, *Appl. Catal., B* 279 (2020), 119390.
- X. Nie, Y. Zhang, Y. Jiang, N. Pan, C. Liu, J. Wang, C. Ma, X. Xia, M. Liu, H. Zhang, X. Li, F. Dong, Efficient extraction of U(VI) from uranium enrichment process wastewater by amine-aminophosphonate-modified polyacrylonitrile fibers, *Sci. Total Environ.* 831 (2022), 154743.
- C.W. Abney, R.T. Mayes, T. Saito, S. Dai, Materials for the recovery of uranium from seawater, *Chem. Rev.* 117 (2017) 13935–14013.
- Q. Meng, X. Yang, L. Wu, T. Chen, Y. Li, R. He, W. Zhu, L. Zhu, T. Duan, Metal-free 2D/2D C₃N₅/GO nanosheets with customized energy-level structure for radioactive nuclear wastewater treatment, *J. Hazard. Mater.* 422 (2022), 126912.
- K. Yu, P. Jiang, H. Yuan, R. He, W. Zhu, L. Wang, Cu-based nanocrystals on ZnO for uranium photoreduction: Plasmon-assisted activity and entropy-driven stability, *Appl. Catal., B* 288 (2021), 119978.
- P. He, L. Zhang, L. Wu, X. Yang, T. Chen, Y. Li, X. Yang, L. Zhu, Q. Meng, T. Duan, Synergistic Effect of the Sulfur Vacancy and Schottky Heterojunction on Photocatalytic Uranium Immobilization: The Thermodynamics and Kinetics, *Inorg. Chem.* 61 (2022) 2242–2250.
- L. Wang, H. Song, L. Yuan, Z. Li, Y. Zhang, J.K. Gibson, L. Zheng, Z. Chai, W. Shi, Efficient U(VI) Reduction and Sequestration by Ti₂CT_x MXene, *Environ. Sci. Technol.* 52 (2018) 10748–10756.
- P. Kumar, E. Vahidzadeh, U.K. Thakur, P. Kar, K.M. Alam, A. Goswami, N. Mahdi, K. Cui, G.M. Bernard, V.K. Michaelis, K. Shankar, C₃N₅: a low bandgap semiconductor containing an azo-linked carbon nitride framework for photocatalytic, photovoltaic and adsorbent applications, *J. Am. Chem. Soc.* 141 (2019) 5415–5436.
- K.M. Cho, K.H. Kim, K. Park, C. Kim, S. Kim, A. Al-Saggaf, I. Gereige, H.-T. Jung, Amine-Functionalized Graphene/CdS Composite for Photocatalytic Reduction of CO₂, *ACS Catal.* 7 (2017) 7064–7069.
- P. Chen, B. Lei, X. Dong, H. Wang, J. Sheng, W. Cui, J. Li, Y. Sun, Z. Wang, F. Dong, Rare-Earth Single-Atom La–N Charge-Transfer Bridge on Carbon Nitride for Highly Efficient and Selective Photocatalytic CO₂ Reduction, *ACS Nano* 14 (2020) 15841–15852.
- L. Luo, W. Chen, S.-M. Xu, J. Yang, M. Li, H. Zhou, M. Xu, M. Shao, X. Kong, Z. Li, H. Duan, Selective Photoelectrocatalytic Glyceral Oxidation to Dihydroxyacetone via Enhanced Middle Hydroxyl Adsorption over a Bi₂O₃-Incorporated Catalyst, *J. Am. Chem. Soc.* 144 (2022) 7720–7730.
- H. Wang, H. Guo, N. Zhang, Z. Chen, B. Hu, X. Wang, Enhanced Photoreduction of U(VI) on C₃N₄ by Cr(VI) and Bisphenol A: ESR, XPS, and EXAFS Investigation, *Environ. Sci. Technol.* 53 (2019) 6454–6461.
- X. Liu, P. Du, W. Pan, C. Dang, T. Qian, H. Liu, W. Liu, D. Zhao, Immobilization of uranium(VI) by niobate/titanate nanoflakes heterojunction through combined adsorption and solar-light-driven photocatalytic reduction, *Appl. Catal., B* 231 (2018) 11–22.
- T. Chen, M. Li, L. Zhou, X. Feng, D. Lin, X. Ding, C. Li, R. Yan, T. Duan, R. He, W. Zhu, Harmonizing the energy band between adsorbent and semiconductor enables efficient uranium extraction, *Chem. Eng. J.* 420 (2021), 127645.
- A. Achour, J. Liu, P. Peng, C. Shaw, Z. Huang, In situ tuning of catalytic activity by thermoelectric effect for ethylene oxidation, *ACS Catal.* 8 (2018) 10164–10172.
- Y. Xu, J. Han, Y. Luo, Y. Liu, J. Ding, Z. Zhou, C. Liu, M. Zou, J. Lan, C.-w. Nan, Y. Lin, Enhanced CO₂ Reduction Performance of BiCuSeO-Based Hybrid Catalysts by Synergetic Photo-Thermoelectric Effect, *Adv. Funct. Mater.* 31 (2021) 2105001.
- X. Chen, L. Liu, Y. Yu, S. Mao, Increasing Solar Absorption for Photocatalysis with Black Hydrogenated Titanium Dioxide Nanocrystals, *Science* 331 (2011) 746–750.
- M. Ye, J. Jia, Z. Wu, C. Qian, R. Chen, P.G. O'Brien, W. Sun, Y. Dong, G.A. Ozin, Synthesis of Black TiO_x Nanoparticles by Mg Reduction of TiO₂ Nanocrystals and their Application for Solar Water Evaporation, *Adv. Energy Mater.* 7 (2017) 1601811.
- X. Han, N. Amrane, A. Murat, Z. Zhang, M. Benkraouda, A GGA+U study of electron localization and oxygen vacancy clustering in rutile TiO_{2-x}, *J. Alloy. Compd.* 855 (2021), 157395.
- J. Gao, J. Xue, S. Jia, Q. Shen, X. Zhang, H. Jia, X. Liu, Q. Li, Y. Wu, Self-Doping Surface Oxygen Vacancy-Induced Lattice Strains for Enhancing Visible Light-Driven Photocatalytic H₂ Evolution over Black TiO₂, *ACS Appl. Mater. Interfaces* 13 (2021) 18758–18771.
- Y. Zhu, J. Li, C.-L. Dong, J. Ren, Y.-C. Huang, D. Zhao, R. Cai, D. Wei, X. Yang, C. Lv, W. Theis, Y. Bu, W. Han, S. Shen, D. Yang, Red phosphorus decorated and doped TiO₂ nanofibers for efficient photocatalytic hydrogen evolution from pure water, *Appl. Catal., B* 255 (2019), 117764.
- Y. Tang, W. Zhou, Q. Shang, Y. Guo, H. Hu, Z. Li, Y. Zhang, L. Liu, H. Wang, X. Tan, T. Yu, J. Ye, Discerning the mechanism of expedited interfacial electron transformation boosting photocatalytic hydrogen evolution by metallic 1T-WS₂ induced photothermal effect, *Appl. Catal., B* 310 (2022), 121295.
- H. Jiang, Z. Xing, T. Zhao, Z. Yang, K. Wang, Z. Li, S. Yang, L. Xie, W. Zhou, Plasmon Ag nanoparticle/Bi₂S₃ ultrathin nanobelt/oxygen-doped flower-like MoS₂

- nanosphere ternary heterojunctions for promoting charge separation and enhancing solar-driven photothermal and photocatalytic performances, *Appl. Catal., B* 274 (2020), 118947.
- [26] H. Huang, Y. Cui, Q. Li, C. Dun, W. Zhou, W. Huang, L. Chen, C.A. Hewitt, D. L. Carroll, Metallic 1T phase MoS₂ nanosheets for high-performance thermoelectric energy harvesting, *Nano Energy* 26 (2016) 172–179.
- [27] W. Huang, X. Luo, C.K. Gan, S.Y. Quek, G. Liang, Theoretical study of thermoelectric properties of few-layer MoS₂ and WSe₂, *Phys. Chem. Chem. Phys.* 16 (2014) 10866–10874.
- [28] A. Achour, K. Chen, M.J. Reece, Z. Huang, Tuning of catalytic activity by thermoelectric materials for carbon dioxide hydrogenation, *Adv. Energy Mater.* 8 (2018) 1701430.
- [29] S.S. Chou, B. Kaehr, J. Kim, B.M. Foley, M. De, P.E. Hopkins, J. Huang, C. J. Brinker, V.P. Dravid, Chemically Exfoliated MoS₂ as Near-Infrared Photothermal Agents, *Angew. Chem. Int. Ed.* 52 (2013) 4160–4164.
- [30] L. Wu, X. Yang, T. Chen, Y. Li, Q. Meng, L. Zhu, W. Zhu, R. He, T. Duan, Three-dimensional C₃N₅/RG0 aerogels with enhanced visible-light response and electron-hole separation efficiency for photocatalytic uranium reduction, *Chem. Eng. J.* 427 (2022), 131773.
- [31] K. Yu, L. Tang, X. Cao, Z. Guo, Y. Zhang, N. Li, C. Dong, X. Gong, T. Chen, R. He, W. Zhu, Semiconducting Metal–Organic Frameworks Decorated with Spatially Separated Dual Cocatalysts for Efficient Uranium(VI) Photoreduction, *Adv. Funct. Mater.* 32 (2022) 2200315.
- [32] R. Shi, H.-F. Ye, F. Liang, Z. Wang, K. Li, Y. Weng, Z. Lin, W.-F. Fu, C.-M. Che, Y. Chen, Interstitial P-Doped CdS with Long-Lived Photogenerated Electrons for Photocatalytic Water Splitting without Sacrificial Agents, *Adv. Mater.* 30 (2018) 1705941.
- [33] W.-D. Liu, D.-Z. Wang, Q. Liu, W. Zhou, Z. Shao, Z.-G. Chen, High-performance GeTe-based thermoelectrics: from materials to devices, *Adv. Energy Mater.* 10 (2020) 2000367.
- [34] Z. Zhou, J. Yang, Q. Jiang, D. Zhang, J. Xin, X. Li, Y. Ren, X. He, Thermoelectric performance of SnTe with ZnO carrier compensation, energy filtering, and multiscale phonon scattering, *J. Am. Ceram. Soc.* 100 (2017) 5723–5730.
- [35] N. Roy, Y. Sohn, D. Pradhan, Synergy of Low-Energy {101} and High-Energy {001} TiO₂ Crystal Facets for Enhanced Photocatalysis, *ACS Nano* 7 (2013) 2532–2540.
- [36] Q. Zhang, Y. Wang, X. Zhu, X. Liu, H. Li, 1T and 2H mixed phase MoS₂ nanobelts coupled with Ti³⁺ self-doped TiO₂ nanosheets for enhanced photocatalytic degradation of RhB under visible light, *Appl. Surf. Sci.* 556 (2021), 149768.
- [37] D. Tang, J. Li, Z. Yang, X. Jiang, L. Huang, X. Guo, Y. Li, J. Zhu, X. Sun, Fabrication and mechanism exploration of oxygen-incorporated 1T-MoS₂ with high adsorption performance on methylene blue, *Chem. Eng. J.* 428 (2022), 130954.
- [38] Z. Li, R. Fan, Z. Hu, W. Li, H. Zhou, S. Kang, Y. Zhang, H. Zhang, G. Wang, Ethanol introduced synthesis of ultrastable 1T-MoS₂ for removal of Cr(VI), *J. Hazard. Mater.* 394 (2020), 122525.
- [39] S. Wu, M.Y. Manuputty, Y. Sheng, H. Wang, Y. Yan, M. Kraft, R. Xu, Flame Synthesized Blue TiO_{2-x} with Tunable Oxygen Vacancies from Surface to Grain Boundary to Bulk, *Small Methods* 5 (2021) 2000928.
- [40] W. Zhang, H. He, Y. Tian, H. Li, K. Lan, L. Zu, Y. Xia, L. Duan, W. Li, D. Zhao, Defect-engineering of mesoporous TiO₂ microspheres with phase junctions for efficient visible-light driven fuel production, *Nano Energy* 66 (2019), 104113.
- [41] X. Wang, W. Ding, H. Li, H. Li, S. Zhu, X. Zhu, J. Dai, Z. Sheng, H. Wang, X. Zhu, Y. Sun, S.X. Dou, Unveiling highly ambient-stable multilayered 1T-MoS₂ towards all-solid-state flexible supercapacitors, *J. Mater. Chem. A* 7 (2019) 19152–19160.
- [42] L. Zhang, X. He, Q. Zhou, X. Hu, Fabrication of 1T-MoS₂ nanosheets and the high-efficiency removal of toxic metals in aquatic systems: Performance and mechanisms, *Chem. Eng. J.* 386 (2020), 123996.
- [43] X. Chen, Z. Wang, Y. Wei, X. Zhang, Q. Zhang, L. Gu, L. Zhang, N. Yang, R. Yu, High Phase-Purity 1T-MoS₂ Ultrathin Nanosheets by a Spatially Confined Template, *Angew. Chem. Int. Ed.* 58 (2019) 17621–17624.
- [44] X. Zhao, Z. Li, J. Zhang, F. Gong, B. Huang, Q. Zhang, Q.-L. Yan, Z. Yang, Regulating safety and energy release of energetic materials by manipulation of molybdenum disulfide phase, *Chem. Eng. J.* 411 (2021), 128603.
- [45] S.S. Nardekar, K. Krishnamoorthy, S. Manoharan, P. Pazhamalai, S.J. Kim, Two faces under a hood: unravelling the energy harnessing and storage properties of 1T-MoS₂ quantum sheets for next-generation stand-alone energy systems, *ACS Nano* 16 (2022) 3723–3734.
- [46] X. Yu, B. Kim, Y.K. Kim, Highly Enhanced Photoactivity of Anatase TiO₂ Nanocrystals by Controlled Hydrogenation-Induced Surface Defects, *ACS Catal.* 3 (2013) 2479–2486.
- [47] W. Zhao, Z. Liu, Z. Sun, Q. Zhang, P. Wei, X. Mu, H. Zhou, C. Li, S. Ma, D. He, P. Ji, W. Zhu, X. Nie, X. Su, X. Tang, B. Shen, X. Dong, J. Yang, Y. Liu, J. Shi, Superparamagnetic enhancement of thermoelectric performance, *Nature* 549 (2017) 247–251.
- [48] R. Fu, Z. Wu, Z. Pan, Z. Gao, Z. Li, X. Kong, L. Li, Fluorine-induced surface metallization for ammonia synthesis under photoexcitation up to 1550 nm, *Angew. Chem. Int. Ed.* 60 (2021) 11173–11179.
- [49] C. Gayner, Y. Amouyal, Energy filtering of charge carriers: current trends, challenges, and prospects for thermoelectric materials, *Adv. Funct. Mater.* 30 (2020) 1901789.
- [50] S.V. Faleev, F. Léonard, Theory of enhancement of thermoelectric properties of materials with nanoinclusions, *Phys. Rev. B* 77 (2008), 214304.
- [51] H. Wan, Y. Li, M. Wang, Q. Zhao, Y. Fu, Y. Chen, P. He, L. Wu, Q. Meng, T. Ma, J. Yang, T. Duan, Boosting efficient U(VI) immobilization via synergistic Schottky heterojunction and hierarchical atomic-level injected engineering, *Chem. Eng. J.* 430 (2022), 133139.
- [52] X. Han, H.M. Stewart, S.A. Shevlin, C.R.A. Catlow, Z.X. Guo, Strain and orientation modulated bandgaps and effective masses of phosphorene nanoribbons, *Nano Lett.* 14 (2014) 4607–4614.
- [53] Z. Zhu, Y. Han, C. Chen, Z. Ding, J. Long, Y. Hou, Reduced graphene oxide-cadmium sulfide nanorods decorated with silver nanoparticles for efficient photocatalytic reduction carbon dioxide under visible light, *ChemCatChem* 10 (2018) 1627–1634.
- [54] Y. Wu, B. Zhu, M. Huang, L. Liu, Q. Shi, M. Akbar, C. Chen, J. Wei, J.F. Li, L. R. Zheng, J.S. Kim, H.B. Song, Proton transport enabled by a field-induced metallic state in a semiconductor heterostructure, *Science* 369 (2020) 184–188.
- [55] X.-D. Wang, Y.-H. Huang, J.-F. Liao, Y. Jiang, L. Zhou, X.-Y. Zhang, H.-Y. Chen, D.-B. Kuang, In Situ Construction of a Cs₂SnI₆ Perovskite Nanocrystal/SnS₂ Nanosheet Heterojunction with Boosted Interfacial Charge Transfer, *J. Am. Chem. Soc.* 141 (2019) 13434–13441.
- [56] R. Kumar, D. Varandani, B.R. Mehta, Nanoscale interface formation and charge transfer in graphene/silicon Schottky junctions; KPFM and CAFM studies, *Carbon* 98 (2016) 41–49.
- [57] M. Hong, Z.-G. Chen, L. Yang, Y.-C. Zou, M.S. Dargusch, H. Wang, J. Zou, Realizing zT of 2.3 in Ge_{1-x-y}Sb_xIn_yTe via Reducing the Phase-Transition Temperature and Introducing Resonant Energy Doping, *Adv. Mater.* 30 (2018) 1705942.
- [58] N. Wang, M. Li, H. Xiao, X. Zu, L. Qiao, Layered LaCuOSe: a promising anisotropic thermoelectric material, *Phys. Rev. Appl.* 13 (2020), 024038.
- [59] J.M. Skelton, L.A. Burton, S.C. Parker, A. Walsh, C.-E. Kim, A. Soon, J. Buckeridge, A.A. Sokol, C.R.A. Catlow, A. Togo, I. Tanaka, Anharmonicity in the High-Temperature Cmcm Phase of SnSe: Soft Modes and Three-Phonon Interactions, *Phys. Rev. Lett.* 117 (2016), 075502.
- [60] R. Abinaya, J. Archana, S. Harish, M. Navaneethan, C. Muthamizhchelvan, S. Ponnusamy, H. Udono, R. Sugahara, Y. Hayakawa, M. Shimomura, Interface driven energy-filtering and phonon scattering of polyaniline incorporated ultrathin layered molybdenum disulfide nanosheets for promising thermoelectric performance, *J. Colloid Interface Sci.* 584 (2021) 295–309.
- [61] M. Qiu, Z. Liu, S. Wang, B. Hu, The photocatalytic reduction of U(VI) into U(IV) by ZIF-8/g-C₃N₄ composites at visible light, *Environ. Res.* 196 (2021), 110349.
- [62] Q. Hao, Zhiqiang Wang, T. Wang, Z. Ren, C. Zhou, X. Yang, Role of Pt Loading in the Photocatalytic Chemistry of Methanol on Rutile TiO₂(110), *ACS Catal.* 9 (2019) 286–294.
- [63] C. Zhao, Z. Chen, J. Xu, Q. Liu, H. Xu, H. Tang, G. Li, Y. Jiang, F. Qu, Z. Lin, X. Yang, Probing supramolecular assembly and charge carrier dynamics toward enhanced photocatalytic hydrogen evolution in 2D graphitic carbon nitride nanosheets, *Appl. Catal., B* 256 (2019), 117867.